Self-pinning of a nanosuspension droplet: Molecular dynamics simulations

Baiou Shi and Edmund B. Webb, III

Phys. Rev. E **94**, 012614 — Published 18 July 2016

DOI: 10.1103/PhysRevE.94.012614

Self-pinning of a nanosuspension droplet: molecular dynamics simulations

Baiou Shi and Edmund B. Webb III

P.C. Rossin College of Engineering and Applied Science,

Lehigh University, Bethlehem, Pennsylvania 18015, USA

Abstract

Results are presented from molecular dynamics simulations of Pb(l) nanodroplets containing dispersed Cu nanoparticles (NPs) and spreading on solid surfaces. Three-dimensional simulations are employed throughout, but droplet spreading and pinning are reduced to two-dimensional processes by modeling cylindrical NPs in cylindrical droplets; NPs have radius $R_{NP} \cong 3\,\mathrm{nm}$ while droplets have initial $R_0 \cong 42\,\mathrm{nm}$. At low particle loading explored here, NPs in sufficient proximity to the initial solid/droplet interface are drawn into advancing contact lines; entrained NPs eventually bind with the underlying substrate. For relatively low advancing contact angle θ_{adv}, self-pinning on entrained NPs occurs; for higher θ_{adv}, de-pinning is observed. Self-pinning and de-pinning cases are compared and forces on NPs at the contact line are computed during a de-pinning event. Though significant flow in the droplet occurs in close proximity to the particle during de-pinning, resultant forces are relatively low. Instead, forces due to liquid atoms confined between the particles and substrate dominate forces on NPs; that is, for NP size studied here, forces are interface dominated. For pinning cases, a precursor wetting film advances ahead of the pinned contact line but at a significantly slower rate than for a pure droplet. This is because the precursor film is a bilayer of liquid atoms on the substrate surface but it is instead a monolayer film as it crosses over pinning particles; thus, mass delivery to the bilayer structure is impeded.

Keywords: modeling; wetting; self-pinning

I. INTRODUCTION

Liquid drops on solid surfaces have garnered tremendous attention for over two centuries [1], owing to their ubiquity in nature and technology. Much has been learned about driving forces dictating the rate at which a drop spreads across a surface [2, 3]; nonetheless, studies continue to demonstrate rich physical complexity inherent in capillary systems [4]. If solid particles are introduced into a spreading drop, underlying driving forces become more complex, challenging our understanding even further. Research in this area has been invigorated by possibilities for advanced materials fabrication through selective deposition of particle suspension drops and subsequent solvent evaporation. In this manner, potential exists to generate ordered arrays of solid particles on surfaces from a relatively inexpensive, large-scale process. Applications for such structures exist in the photonic, microelectronic, and biotechnology industries [5-8].

Much of the initial attention on suspension drops arose, however, from a more commonplace question: why do coffee drops form ring-shaped stains upon evaporation instead of circles [9, 10]? It has been shown that, as a suspension drop evaporates, it does so most rapidly from its edges. As the contact line initially retracts, outward flow develops to carry solvent to the region of highest evaporation; this flow also carries suspended particles to the outer edge, leading to contact line pinning by the particles, or self-pinning. Subsequent evaporation and flow causes particle pile-up at the pinned drop edge, leading to a ring-shaped stain, rather than a circle [10]. Contact line pinning has been extensively considered during contact line retreat due to solvent evaporation [11-18]; this is partly because self-pinning is a phenomenon that is highly relevant to manufacturing efforts based on deposition and subsequent evaporation. Suspended particles can also influence advancing contact lines; competing observations have been made with some suspension systems showing increased spreading kinetics and others showing decreased kinetics [19, 20]. The former observation was attributed to a disjoining pressure induced by particle ordering near the contact line; the latter

observation was associated with increased surface tension and fluid/solid friction. It is clear that more must be learned to enable accurate predictions of what specific behavior will be observed for varying suspension droplet wetting scenarios.

Self-pinning was recently explored experimentally and a mechanism was advanced based on capillary force due to particle confinement at the contact line [21]. Two relevant forces on a potentially pinning particle were identified: a spreading force F_S and a capillary force F_C (a drag force was also discussed but demonstrated to be of negligible value compared to F_S and F_C). The spreading force acts to move the liquid front (and particles at the contact line) outward in the radial (spreading) direction and is $F_S = 2\pi RS$, where R is the wetted region radius and $S = \gamma_{sg} - \gamma_{sl} - \gamma_{lg}$; γ_{sg}, γ_{sl}, and γ_{lg} are the solid/gas, solid/liquid, and liquid/gas interfacial tensions, respectively. When the contact angle is greater than the equilibrium value, a latent spreading force F_S can be considered that is greater than zero and drives both contact line (and particle) advancement. For a pinned contact line, the authors postulated that the capillary force acts inward in the radial direction, where the force due to each particle entrained to the contact line is $F_C = 2\pi r\gamma_{lg}(cos\theta)^2$ (r is the pinning particle radius and θ is the apparent contact angle). In Ref. 21 and throughout this work, contact angles are considered between the vapor/liquid and liquid/solid interfaces (i.e. on the liquid side of the vapor/liquid interface). By calling the number of particles entrained to the contact line N and equating F_S and NF_C, a critical contact line particle packing for self-pinning was predicted and verified in experiments [21]. Similar approaches have been advanced by other authors. For example, in addition to considering forces due to viscous drag and capillary interaction between the liquid front and particle, one prior study also advanced expressions for the force exerted on potentially pinning particles by an underlying substrate [22]. Again by establishing a force balance, authors were able to predict conditions for contact line pinning. In both of these cited works it was hypothesized that nanometer scale particles can get closer to contact lines, facilitating easier self-pinning. It is clear that predicting the behavior of particles entrained into advancing contact lines requires thorough understanding of constitutive forces in such wetting systems.

Recent studies have shown the capability of atomic scale molecular dynamics (MD)

simulations to reveal underlying driving forces dictating changes in surface tension and viscosity for nano particle suspensions [23]. MD simulations have been used to study particle ordering during suspension evaporation in liquid film geometries [24]. In separate work, MD simulations were used to explore particle ordering during evaporation of suspension droplets [16]. Droplet spreading (i.e. contact line advance) was also recently explored for nano particle suspension drops via MD simulations [20]. While these works have clearly demonstrated the important role that atomic scale modeling plays in studying suspension behavior, no results have been advanced using such simulations to directly examine suspended particles entrained into advancing contact lines during successful versus failed self-pinning attempts.

For atomic scale MD simulations of droplet wetting, some benefits have been identified for using metallic material models such as the embedded atom method (EAM) [25]. The multibody nature of such atomic interaction models means that simple (monoatomic) liquids can be studied and that they will exhibit negligible vapor pressure. With no vapor phase present (and the corresponding absence of a re-adsorbed wetting layer on the substrate), analyzing mechanisms of contact line advancement and characterizing the morphology of the contact line region are somewhat simplified. Additionally, embedded atom method potentials have been advanced that describe certain metallic systems with very good accuracy, compared to experimental data and density functional theory based calculations. Metallic droplet spreading is germane to broad manufacturing interests as it underlies material joining processes like soldering and welding [36]; furthermore, incomplete melting and impurities can lead to solid particles suspended in spreading liquids [37]. Thus, motivation exists to use MD simulations to explore self-pinning for metallic systems at the atomic scale. Ideally, results so obtained will help elucidate not only metallic system behavior but also provide generalizations to other material systems.

Here, self-pinning of advancing contact lines by nano particles is explored using MD simulations. The model metallic material system used for liquid, particles, and substrate is such that, for identical solid/liquid chemistry, different spreading kinetics and advancing contact angle θ_{adv} are observed depending on the crystal structure of the substrate surface. In cases of identical particle loading and initial configuration in the

drop, self-pinning is observed for low θ_{adv} whereas it is not for high θ_{adv}. Mechanisms leading to pinning in the low θ_{adv} case are compared to those that manifest liquid front separation from the entrained particle (i.e. de-pinning) in the high θ_{adv} case. Forces on particles are computed during pinning and de-pinning to provide further interpretation of mechanisms controlling contact line behavior. Results demonstrate that, for nanometer size particles explored here, forces due to liquid flow are small relative to those manifesting from interactions at the particle/substrate interface.

II. MOLECULAR DYNAMICS SIMULATION PROCEDURE

MD simulations employed embedded atom method [25] interatomic potentials for describing interactions between liquid Pb and solid Cu (both suspended particles and substrate surfaces were modeled to be Cu); specific potentials used to describe Cu-Cu, Pb-Pb, and Cu-Pb interactions were previously advanced and have been demonstrated to describe this material system with very good accuracy [25-28]. Nonetheless, rather than to connect with a specific material composition, the Cu-Pb system was chosen here based on more general attributes of metallic systems, as described in the preceding section. Liquid metals modeled via EAM potentials typically exhibit relatively high surface tension γ_{lg} and low viscosity η, in accord with experimental observations on these materials. These quantities were previously computed for the model of Pb(l) used here and at the same T = 700 K as is modeled here; they are $\gamma_{\mathrm{lg}} = 0.574 \pm 0.038$ J/m^2 and $\eta = 2 \pm 0.2$ mPa·s [32].

This system was additionally chosen as prior studies have revealed interesting wetting behavior for Pb(l) drops on Cu. Despite identical chemistry, both the advancing contact line morphology (i.e. θ_{adv}) and the advancing contact line velocity differ significantly for Pb(l) wetting Cu(001) versus Cu(111). Lower θ_{adv} and higher spread velocity are observed on Cu(111) and this is most evident during inertial stage wetting [28, 32]. Thus, this system provides an opportunity to examine the role of θ_{adv} on determining likelihood for self-pinning. Experimentally, this system has been found to be partially wetting; on polycrystalline Cu surfaces the equilibrium contact angle was observed to

vary with T from $\theta_0 = 45°$ at $T = 600$ K to $\theta_0 = 20°$ at $T = 1000$ K [33]. Prior simulation studies using the Pb/Cu model used here showed that, for $T = 700$ K, $\theta_0 = 30°$ on Cu(001) and $\theta_0 = 20°$ on Cu(111) [28]. In both experiments and simulations, an atomically thick precursor film was observed to spread ahead of advancing droplet contact lines. A potential drawback to studying wetting in metal systems is that many such chemical combinations exhibit some form of reactive wetting where the chemistry and/or morphology of the solid/liquid interface change with time. However, in agreement with experiment, Pb and Cu in this model are relatively immiscible; thus, solid/liquid interfaces in the model remain relatively sharp.

Figure 1 shows two views of a typical simulation configuration at time $t = 0$. Fully three dimensional simulations were employed throughout; however, to reduce the spreading geometry to two dimensions, liquid cylinders were brought into contact with solid surfaces where the length of the cylinder along its axis (i.e. in the y direction) was identical to the periodic dimension of the simulation cell along y (the same was true for the solid surface). Thus, two independent contact lines advanced in positive/negative x and results were averaged along y to collapse spreading analyses into the xz plane. Despite this being a model of an infinite length liquid cylinder, the relatively small periodic dimension of the simulation cell along y suppressed Rayleigh instabilities in the liquid while also reducing computational cost and permitting study of relatively larger drops. Suspended nano particles were also cylinders, akin to what was done with the liquid drop; at two positions in the top-down view of Fig. 1, particles can be seen that partially protrude out of the surface of the drop and it is obvious they span the simulation dimension in y. Particle insertion into the droplet is described below. Note this is different from recent simulations that also employed cylindrical drops but spherical particles [20]. Here, both spreading and pinning were effectively reduced to 2D processes, explored via 3D simulation ensembles. While motivation exists to explore our described geometry, quantitative differences should be expected between results presented here and what occurs for 3D (i.e. spherical) droplet spreading. For example, herein, a single suspended particle can fully span one of the contact lines; thus, it is not possible to address particle packing at the contact lines here, except in the limits of zero

packing and fully packed. Therefore, focus here is on differences observed between spreading on the two substrate surfaces and care is exercised when interpreting results in terms of spherical droplet behavior.

All results presented here were from isothermal ensembles with $T = 700$ K, which is $\sim 10\%$ greater than the liquid melting point and just over half the solid melting point. Simulation time step throughout was 1 fs and the MD code LAMMPS was used for all simulations [29]. Cu substrates modeled were subject to periodic boundary conditions in x and y with the periodic repeat length of the simulation cells $L_x \sim 300$ nm and $L_y \sim 5$ nm. Substrate L_x was chosen to permit significant droplet spreading without reaching the edge of the simulation cell; L_y was chosen as ten times the EAM interaction model cutoff distance. Because spreading (and pinning) are effectively 2D processes for the geometry modeled here, this L_y value balances competing desires to have sufficient averaging along the cylindrical axis dimension while also to keep computational cost constrained. Since L_y was dictated by the solid substrate lattice constant and the crystallographic surface orientation, this dimension differed a small amount for (001) versus (111) substrates. Solids were initially equilibrated in fully three dimensional periodic ensembles at the zero pressure lattice constant and with appropriate unit cell rotation to have either the Cu(001) or Cu(111) direction along z. For all equilibration runs, the system was identified to be at equilibrium via temporal analysis of potential energy, pressure, and other system properties. Following the initial bulk solid equilibration, periodic boundary conditions were removed along the z direction, forming two free surfaces for each Cu substrate. Substrates had thickness in z equal to 5 nm, with ~ 1 nm of thickness at the free surface in negative z held rigid for all subsequent calculations to prevent total system drift in z. To minimize computational expense, L_z should be minimized; the value used here permits the presence of a constraining frozen region (as described). In addition, as described further below, dynamic substrate atoms are partitioned along z so that a sufficiently large region of the substrate is subject to a temperature control algorithm, or thermostat, to maintain essentially isothermal spreading. Lastly, a region of substrate atoms in closest proximity to the free surface on which spreading occurs is not subject to a thermostat to

prevent artificial influences on observed droplet spreading behavior.

Three dimensional periodic slabs of liquid were equilibrated at the zero pressure density for the desired T. To reach proper liquid density during equilibration runs, L_x and L_z were allowed to vary while L_y was constant as given by the corresponding substrate's L_y. After liquid slab equilibration, cylinders (with cylindrical axis along y) were extracted from the atomic ensembles and re-equilibrated in free space. Two separate drops were thus formed with nominally identical properties but slightly different L_y. Following liquid drop equilibration in free space, the radius of cylindrical drops was determined from plots of number density as a function of radial distance from the cylindrical axis, averaging all data along the cylinder axis in y; the radius was defined as the point on the radial density profile where the plot decreased to half the average density in the bulk liquid. The initial droplet radius was $R_0 = 42$ nm in all cases studied here; particle insertion into the drops and subsequent re-equilibration (described below) did not change R_0 for particle concentration explored here. In a prior work by the current authors on inertial stage wetting, it was demonstrated that droplets simulated via MD gave results in excellent agreement with predictions from continuum scale fluid dynamics theory, so long as droplet radius was of order 10-20 nm or larger [32]. Similarly, prior work by other authors for MD simulations of suspension droplets showed that particle behavior during spreading only agreed with continuum scale predictions for drops of order 15 nm or larger [16]. Droplet size modeled here was thus selected to be somewhat more than two times this minimum size identified by prior works. This again balances a desire for longer spreading duration to analyze, against a desire to minimize computational expense.

To maintain a three dimensional simulation geometry but with both spreading and pinning effectively reduced to two dimensional processes in the xz plane, cylindrical particles were inserted into cylindrical drops. A feature unique to studying self pinning in an effectively 2D geometry is that a single particle entrained into the contact line has the capability to drive self pinning. A cylindrical 'particle' was initially extracted from a solid slab used to form a Cu substrate. The nominal extraction radius was ≤ 3 nm; copies of this model particle were then inserted into the drop in multiple, random

locations. Particle size was chosen somewhat heuristically to be approximately one tenth of the modeled droplet size. Insertion was done so as to ensure that all atoms in a given inserted particle were outside the interaction range of atoms in other particles at $t = 0$; furthermore, particles inserted near the drop edge were required to have at least 75% of the particle's volume inside the drop. To insert a particle, a cylinder of liquid atoms was extracted from the drop using a radial cut-off around the determined insertion point; the cut-off was chosen to ensure that, upon merging a copy of the particle into the drop, the closest separation distance between a drop atom and a solid particle atom was equal to the equilibrium separation distance observed at planar solid/liquid interfaces for this system [34]. After the desired number of particles was inserted, nanosuspension drops were re-equilibrated in free space. Within a few tens of ps after starting these simulations, a small number of particle atoms dissolved into the liquid as initially cylindrical particles rapidly developed facets on low index crystallographic planes. Equilibration of nanosuspension drops was thus relatively quick, relative to simulation time scales. After faceting, following equilibration, particle radius was $r \leq 3$ nm. For results here, 2, 10, or 20 particles were inserted giving volume percent loadings $\phi \sim 0.8\%, 4\%,$ and 8%, respectively. For each case studied, the same (pseudo) random positions were used for particle insertion in both drops. Thus, nominally identical, equilibrated nano suspension drops were prepared for joining with either a Cu(001) or Cu(111) substrate. Spreading simulations were also run for drops with no suspended particles.

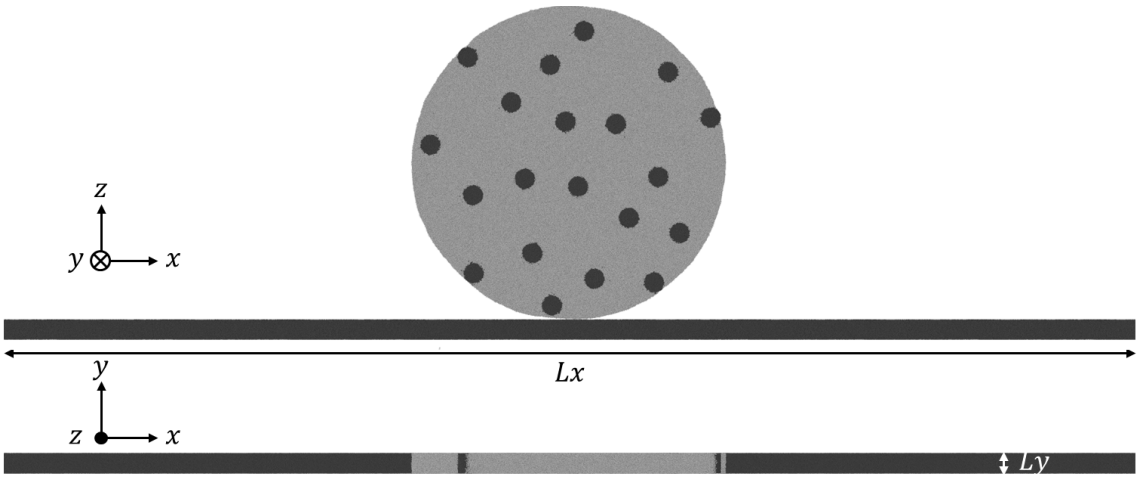

FIG. 1. Two orthographic projection views of a simulation configuration at time $t = 0$ (Pb atoms are light grey; Cu atoms are dark grey). The image is for a $R_0 = 42$ nm drop with 20 Cu particles in contact with the (001) surface of Cu. The spreading direction is x, the free surface normal direction is z, and the droplet's (and particles') cylindrical axes are along y. The periodic repeat lengths of the simulation cells are $L_x = 300$ nm and $L_y = 5$ nm.

Following a drop's equilibration, it was merged into a simulation cell with the desired substrate for subsequent wetting simulations. Drops were inserted adjacent to substrates in positive z such that the closest distance between a drop atom and a substrate atom at $t = 0$ was equal to the equilibrium separation distance observed in planar solid/liquid interface simulations. To maintain isothermal spreading, substrate atoms at least 1 nm from the wetted surface were subject to a thermostat algorithm (excluding rigid substrate atoms at the inactive free surface); all other dynamic atoms were integrated in a constant energy ensemble. This prevented the thermostat algorithm from altering flow behavior in the spreading drops. It was verified that T throughout the drop and substrate (and for all time simulated) did not deviate from $T = 700$ K by more than ~ 15 K.

To characterize wetting kinetics the extent of drop spread in x was computed for both advancing contact lines, averaging all data along y. This was done also as a function of distance from the solid free surface into the drop so that kinetics of precursor wetting films were distinguished from droplet wetting kinetics. The specific method for computing droplet $x(t)$ for varying height above the substrate has been presented previously [32]; in the absence of particles, this method also permits straightforward computation of dynamic contact angle $\theta(t)$. The presence of particles entrained to the contact line complicates the computation of both $x(t)$ and $\theta(t)$ because it is more challenging to define the edge of the liquid front; this will be discussed further below. To characterize flow in drops, velocity vector profiles were computed by assigning atoms to bins according to an atom's xz coordinates at a given t; bins were 1 nm on edge and spanned the system in y. After 10 ps, the xz coordinates of all atoms that were in a given bin were used to compute the aggregate center of mass displacement (and

velocity) for that bin; this analysis time was chosen somewhat heuristically and it balanced a desire for high temporal resolution with a need for sufficient time passage to give definitive results for flow velocity.

III. RESULTS AND DISCUSSION

Figure 2 shows time evolutions for spreading of $\phi = 0$ and $\phi = 8\%$ droplets on the Cu(001) surface; a similar comparison is given for spreading on the Cu(111) surface in Fig. 3. To characterize wetting kinetics the extent of spread versus time $x(t)$ is shown in Fig. 4 for all systems studied; data were obtained from the edge of the drop, making certain to compute the edge position above the two-layer precursor film observed to form in these systems. Thus, kinetic data are indicative of droplet spreading and not precursor film advancement. For all cases explored herein, events at both contact lines for a given case were essentially identical; as such, $x(t)$ data for the two contact lines in each system were averaged to produce plots in Fig. 4.

Spreading in the absence of suspended nano-particles is considered first. As has been previously observed for this system, it can be seen here that, during the earliest stages of spreading, $\theta_{adv} \sim 60^{o}$on Cu(111) was lower than $\theta_{adv} \sim 90^{o}$ on Cu(001); furthermore, spreading kinetics for the lower θ_{adv} case were distinctly faster. It has been previously shown that this difference in contact line morphology manifests from the very onset of spreading in these two systems and that the decreased advancing contact angle on Cu(111) stems from the propensity for rapid precursor film formation and advancement in this system [32]. Indeed, in Fig. 3c for $\phi = 0$ the precursor film is already evident and has extended ~10 nm ahead of the droplet edge on Cu(111). As is commonly observed for low viscosity, high wettability liquids, wetting of Pb(l) on both Cu(001) and Cu(111) is initially characterized by an inertial wetting regime of very rapid spreading; this is followed by a slower spreading regime wherein dynamics are governed by viscous effects (hydrodynamic theory) and/or contact line phenomena (molecular-kinetic theory). It is during inertial wetting that different kinetics manifest on the different crystallographic surfaces. Contact line velocity following the inertial regime is similar for $\phi = 0$ drops on Cu(001) and Cu(111) [32]. For the $R_0 = 42$ nm drops studied here, the

inertial/capillary time scale is $T \sim \sqrt{\rho R_0^3 / \gamma_{lg}} \sim 1.2$ ns, where ρ is the liquid density; further, the inertial regime has been demonstrated to persist in time out to $\sim 2T$. Thus, images in Figs. 2b and 3b are from during inertial spreading while images in Figs. 2c and 3c are well after inertial spreading is complete.

Figures 2 and 3 show that, for the earliest stages of spreading on both Cu(001) and Cu(111), there is little difference between the overall drop morphology for $\phi = 0$ versus $\phi = 8\%$ (θ_{adv} for $\phi = 8\%$ suspension droplets on both Cu(001) and Cu(111) were $\sim 10^\circ$ higher than observed for $\phi = 0$). Kinetic data in Fig. 4 further bear this out, showing that, for spreading on either Cu(001) or Cu(111), $x(t)$ is essentially independent of ϕ out to $t \sim 1$ ns for all ϕ studied here. For $\phi = 8\%$ cases on both Cu(001) and Cu(111), particles were entrained to both contact lines during early stages of wetting. Flow rate to the advancing contact line at early time was sufficiently large in both cases to ensure particles were delivered there; as will be discussed below, this was also dependent on initial particle position in the drop. Focusing on the Cu(001) system in Fig. 2, for $\phi = 8\%$, detachment occurred for both advancing contact lines sometime between t = 1 ns and t = 4 ns; in this case, no self-pinning was observed, despite the presence of entrained particles. In Figure 2c, the images at t = 4 ns for $\phi = 0$ and $\phi = 8\%$ on Cu(001) show that a small difference existed between the total extent of spread for the two systems, with the $\phi = 0$ case having advanced somewhat farther. Kinetic data in Fig. 4 support this description; furthermore, the inflection in $x(t)$ for $\phi = 8\%$ that occurs over the time from $t = 1$ ns to $t = 3$ ns is indicative of de-pinning in this system. This will be described in greater detail below.

Examining results in Fig. 3 for spreading on Cu(111), it can be seen that both advancing liquid fronts remained bound to particles for $\phi = 8\%$. Images at t = 4 ns for $\phi = 0$ and $\phi = 8\%$ in Fig. 3c show that, for $\phi = 0$, both contact lines advanced significantly farther than the pinned contact lines in the $\phi = 8\%$ case on Cu(111). This is corroborated by data in Fig. 4 that shows $x(t)$ for $\phi = 8\%$ is flat after $t \sim 3$ ns, illustrative of a pinned contact line. To emphasize pinning for the nanosuspension droplet on Cu(111), Figs. 5a and 5b compare the $\phi = 0$ case to the $\phi = 8\%$ case at t = 7 ns. In the absence of particles, the droplet continues to spread on Cu(111), albeit

increasingly slowly as it approaches its equilibrium contact angle θ_0 = 20°. However, for $\phi = 8\%$ on Cu(111), it can be seen that, once it becomes pinned, the contact line remains immobile throughout the remainder of the simulation. Considering a cylindrical cap construction to the overall droplet morphology in the pinned case, the apparent pinned contact angle is $\theta_{pin} \sim 50°$. However, because of the self-pinning particle entrained to the contact line, it is important to more carefully examine structure near the contact line and this is discussed further below. Figure 5c shows the $\phi = 8\%$ case on Cu(001) at t = 10 ns; though spreading on the Cu(001) surface is slower, this images bears out that the nanosuspension drop on Cu(001) eventually spreads to a greater extent than the pinned nanosuspension drop on Cu(111). Though the $\phi = 0$ case on Cu(001) is not shown in Fig. 5, the small difference between spreading extent that existed after depinning persisted throughout the remainder of the simulations.

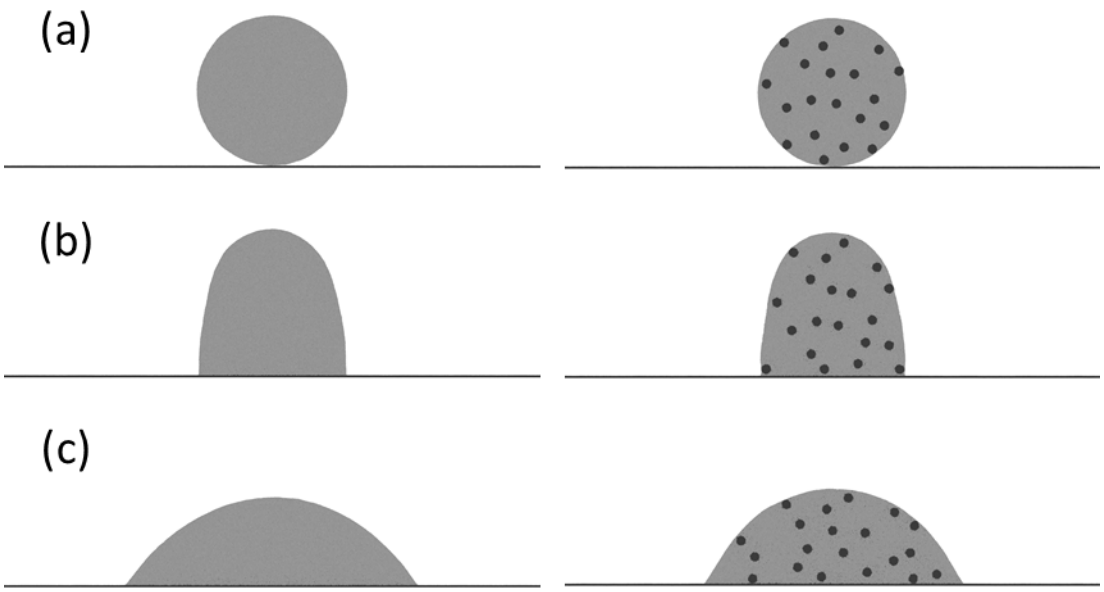

FIG. 2. Comparison between simulations of (left) a pure Pb(l) drop ($\phi = 0$) and (right) a Pb(l) drop containing 20 particles ($\phi = 8\%$) wetting Cu(001) substrates: (a) $t = 0$; (b) $t = 1ns$; (c) $t = 4ns$. In all simulation renderings, light (dark) atoms are Pb (Cu) and only a portion of the substrate is shown; graphics are rendered using AtomEye [30].

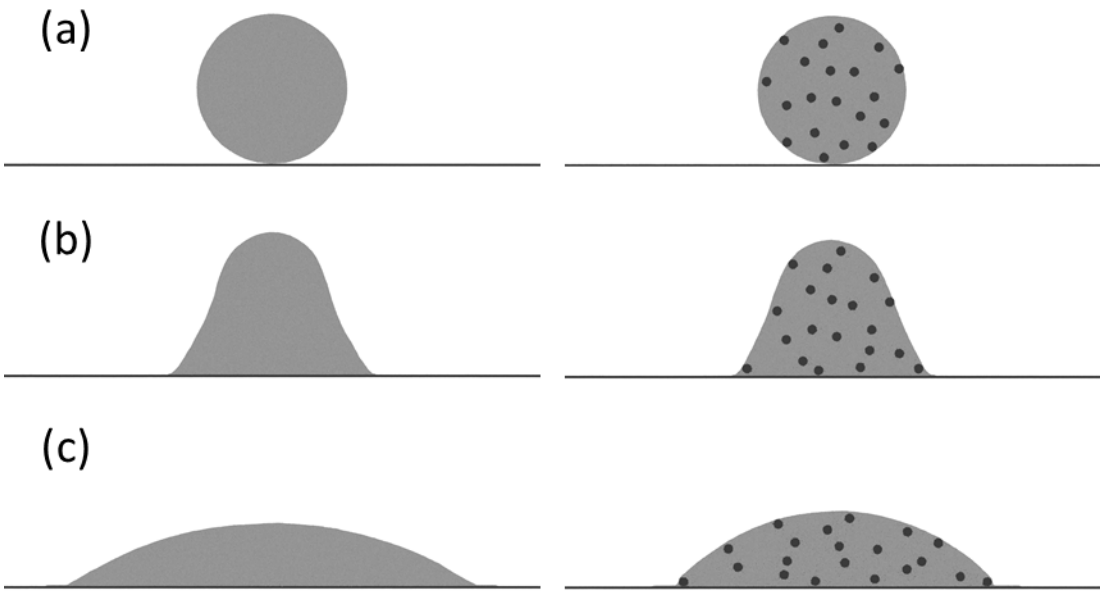

FIG. 3. Comparison between simulations of (left) a pure Pb(l) drop ($\phi = 0$) and (right) a Pb(l) drop containing 20 particles ($\phi = 8\%$) wetting Cu(111) substrates: (a) $t = 0$; (b) $t = 1\text{ns}$; (c) $t = 4\text{ns}$. In all simulation renderings, light (dark) atoms are Pb (Cu) and only a portion of the substrate is shown; graphics are rendered using AtomEye [30].

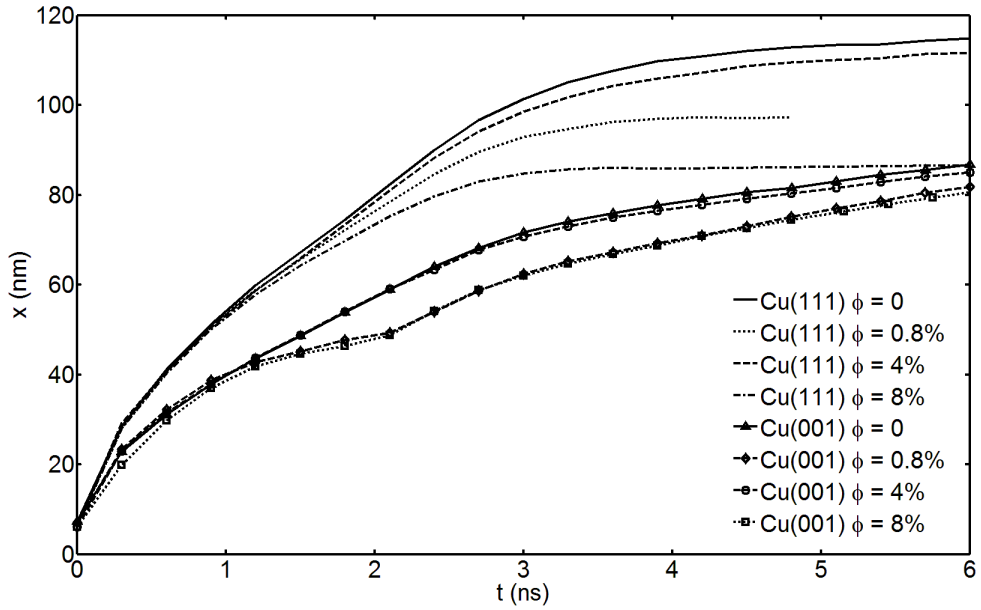

FIG. 4. Extent of droplet spread in x versus time t. Data are presented for Pb droplets wetting Cu (001) and Cu(111) for varying particle loading: $\phi = 0,\ 0.8\%, 4\%,$ and 8%.

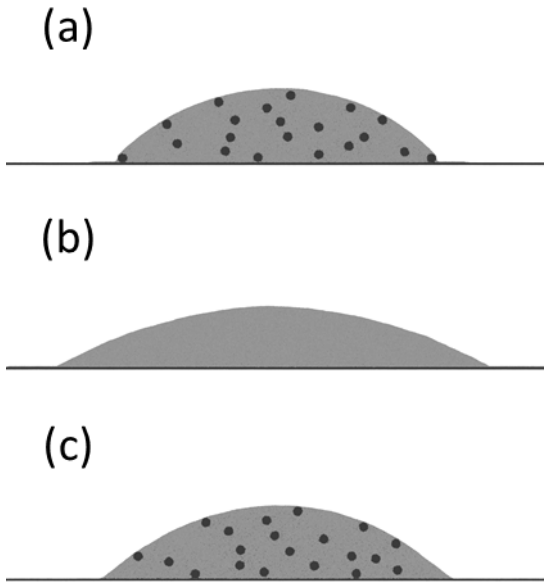

FIG. 5. Simulation snapshots of systems at later times: (a) $\phi = 8\%$ droplet wetting Cu(111) ($t = 7$ns); (b) $\phi = 0$ droplet wetting Cu(111) ($t = 7$ns); (c) $\phi = 8\%$ droplet wetting Cu(001) ($t = 10$ns).

Figure 4 shows data for droplets with $\phi = 4\%$ wetting both Cu(001) and Cu(111); in those cases, due to the random positions selected upon inserting the particles, no particles were entrained to the advancing contact lines during spreading. Thus, $x(t)$ data for $\phi = 4\%$ on both Cu(001) and Cu(111) are very similar to what was observed for $\phi = 0$ on both of these surfaces. At later time after intertial spreading is complete, a small reduction in spreading kinetics can be observed for $\phi = 4\%$ compared to $\phi = 0$ on both Cu(001) and Cu(111); on Cu(001), this reduction is very small. Since this difference emerges as viscous dissipation becomes a more dominant driving force determining spreading kinetics, this indicates that particle inclusion at this low loading causes a small increase to the droplet's effective viscosity. Otherwise, particle inclusion for $\phi = 4\%$ had little effect on spreading behavior because no particles were entrained into the advancing contact lines.

At particle loadings explored here, entrainment to the advancing contact line is a result of particles being in the correct region of the drop at time zero. To test this, simulations were repeated for wetting on both Cu(001) and Cu(111) but with only two particles

inserted into each droplet ($\phi = 0.8\%$). The particles were inserted into the identical positions as those two particles that were entrained into the contact line for $\phi = 8\%$. Because of the symmetry in our simulations, two particle insertion represents the dilute limit of loading since only a single particle exists on either side of the symmetry plane. As shown in Fig. 4, results for the dilute limit on Cu(001) were essentially identical to what was observed for $\phi = 8\%$. The two particles inserted were again entrained into the contact line, began to slow the particle front around t = 1 ns, and were subsequently left behind after the advancing liquid front detached from the entrained particles. On Cu(111) results for the dilute limit were the same in the sense that contact line pinning was observed like it was for the $\phi = 8\%$ case. However, during the latter half of inertial regime spreading, differences in spreading kinetics for $\phi = 0.8\%$ and $\phi = 8\%$ began to emerge with the dilute limit system spreading somewhat faster than the $\phi = 8\%$ system. This difference is again indicative of a greater effective viscosity for the higher loading system. Nonetheless, the primary result that pinning occurs on Cu(111) persists. The reason the difference is smaller between kinetics for the dilute limit and $\phi = 8\%$ on Cu(001) is because entrained particles in those systems attempt to pin the contact line earlier than on Cu(111); data in Fig. 4 show that dramatic deceleration of the liquid front occurs starting about half way through the inertial spreading regime on Cu(001). The de-pinning events dominate spreading kinetics from $t \sim 1$ ns to $t \sim 3$ ns; thus, viscous influences on spreading kinetics do not emerge until later in time. Indeed, at the latest time shown in Fig. 4, spreading kinetics for the dilute limit $\phi = 0.8\%$ droplet on Cu(001) are a very small amount faster than for the $\phi = 8\%$ droplet.

Other than repeating the two particle positions that led to entrainment for the $\phi = 8\%$ case, no further attempt was made to assess more rigorously the region in the drop where a particle can be inserted such that it will then be entrained into the contact line. By doing so, one could compute the corresponding volume (or area) fraction and use that to make arguments about the probability for particle entrainment to the contact line at varying loading levels. However, as loading increases, particle/particle interaction effects also become more pronounced such that more complex behavior should be expected. Successful particle entrainment to the contact line is also likely particle size

dependent. Thus, remaining focus here is on revealing behavior observed near the contact line for the pinning versus de-pinning cases.

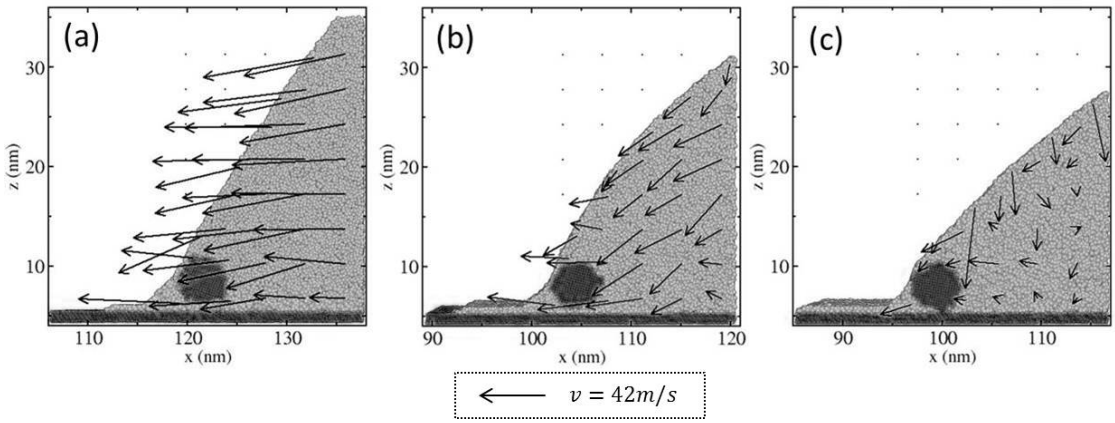

FIG. 6. Contact line region images and fluid flow behavior for a pinning case on Cu(111). Data are shown at (a) $t = 1.5$ ns (early time of spreading), (b) $t = 2.5$ ns (right before pinning), and (c) $t = 3.2$ ns (when self-pinning is complete). All vector magnitudes adopt the scale depicted in the legend.

Figure 6 shows the contact line region for one of the advancing liquid fronts in a pinning case on Cu(111); as described in the procedure section, flow velocity plots have been created for the times shown and corresponding vectors are overlayed on the simulation snapshots. Though only one contact line is shown, events at the other three pinning contact lines were nearly identical to what is shown here. The largest velocity vector in Fig. 6 corresponds to $v = 79$ m/s and all vectors are scaled according to the figure legend. Significant spreading velocity exhibited on Cu(111) during inertial spreading is evident in Fig. 6a; it can further be seen that prior to pinning, a complete liquid film existed between the substrate and particle and this abetted the particle moving in concert with the liquid front. In Fig. 6b, an image is shown when the particle first began to experience interactions with the underlying substrate; because both particles and substrate were modeled as Cu, strong bonds could form between particle and substrate atoms. At the later point in time shown in Fig. 6b, significant flow lateral to the

substrate seen in Fig. 6a has been replaced with more inclined flow that is oriented toward the contact line. Nonetheless, fairly fast flow velocities are still observed. Over the next 0.7 ns, flow velocities adjacent to the contact line are shown in Fig. 6c to diminsh dramatically in accord with halting of the liquid front advancement. Careful examination of the particle/substrate interface shows that a sufficient number of Cu-Cu bonds have formed there to partially eliminate the liquid film between particle and substrate. This halts particle advancement, leading to contact line pinning.

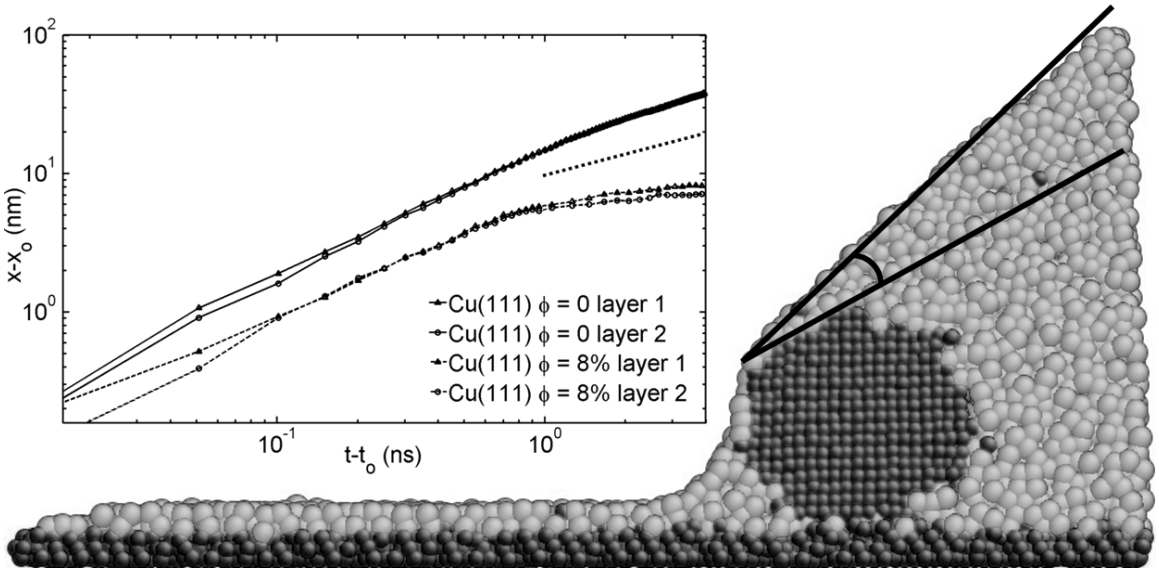

FIG. 7. A plan view image of a magnified contact line region at late time (t = 7 ns) for the $\phi = 8\%$ pinning case on Cu(111). The inset shows a log-log presentation for precursor film kinetic data where both a starting time $t_0 = 3$ ns and starting position x_0 for the precursor spreading regime have been used (see text). Data are presented for the two layers of Pb atoms in the film for $\phi = 0$ and $\phi = 8\%$. The dotted line segment shown at late time illustrates a slope of ½.

Figure 7 shows a magnified image of the same contact line region shown in Fig. 6 but for later in time. As was presented above, the apparent contact angle for the $\phi = 8\%$ pinned cases is $\theta_{pin} \sim 50°$ (for the dilute limit case, the apparent contact angle at both contact lines was a little less $\theta_{pin} \sim 45°$). However, as shown in Fig. 7, structure at the pinned contact line was more complex in that particle faceting manifested an inclined

solid plane of atoms at the very edge of the liquid front. As indicated schematically in the figure, this implies that the contact angle of the liquid front on the particle is very near the equilibrium value for this system. Thus, the combination of a low advancing contact angle with faceted particles entrained into the contact lines means that, when the particles become bound to the underlying substrate, the liquid is able to adopt the equilibrium contact angle on the particle, reducing the local driving force for spreading to zero. An additional observation from Fig. 7 is that, even at this later time, the interface between the particle and the underlying substrate is not pure Cu but instead contains some liquid atoms. Despite pinning, the bilayer precursor film that has been previously studied for this wetting system is still observed in Fig. 7 to advance across the Cu(111) surface. However, it can also be seen that, as liquid film atoms transport across one facet of the particle, they do so as a monolayer; thus, precursor film kinetics in pinned systems are significantly reduced from what is observed for droplets with no particles.

Prior work has shown that the bilayer precursor film advances ahead of pure drops with $x(t) \sim t^{1/2}$ kinetics and the inset of Fig. 7 gives evidence of the same here. The inset shows $x(t - t_0)$ for the first two layers of Pb atoms above the substrate surface, where t_0 indicates the onset of the precursor spreading regime (i.e. when the precursor emerges as a distinct spreading entity from the drop). A similar adjustment is made to account for the starting position of the precursor film at t_0, x_0. This is necessary to distinguish power law kinetics for the precursor film from those exhibited by the entire drop during the inertial spreading regime. Recall that data for droplet kinetics in Fig. 4 were obtained by tracking the x position of the edge of the third layer of Pb atoms above the substrate; this was done to distinguish the main drop edge from the precursor film. Nonetheless, until the inertial regime concluded, the position of the front of the first three layers of Pb atoms was nearly identical. Thus, the precursor film did not advance ahead of the droplet edge until after conclusion of the inertial regime; since inertial spreading was observed until approximately $2T$ (two times the inertial/capillary time scale), $t_0 = 2.5T = 3$ ns. A line with slope ½ is imposed on the inset figure, bolstering evidence for power law behavior in the absence of a pinning particle. However, that does not appear to be the case for the precursor film advancing ahead of the pinned liquid front. Given that the monolayer liquid film on the particle facet must provide mass

transport to the advancing bilayer film, it seems intuitively reasonable that $t^{1/2}$ kinetics for precursor films would be disrupted in pinned cases. The inset to Fig. 7 bears this out.

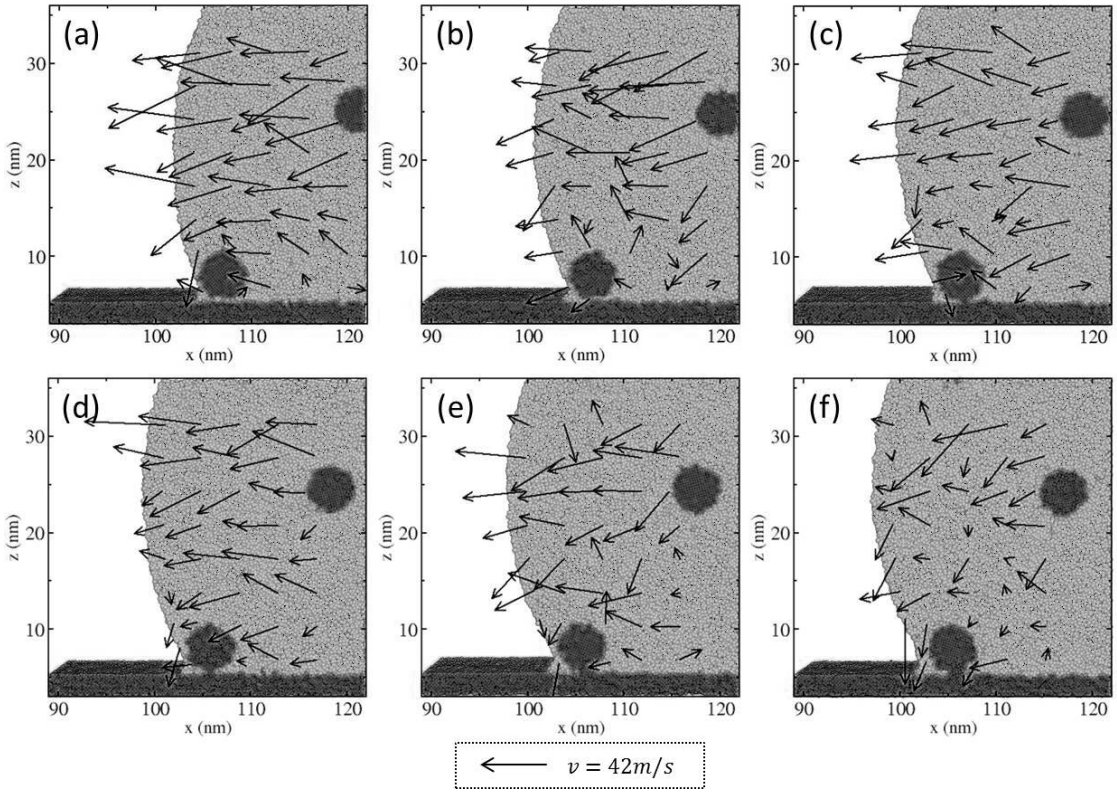

FIG. 8. Contact line region images and fluid flow behavior for a de-pinning case on Cu(001). Images show the advancing liquid front as it starts detaching from the particle: (a) $t = 1.6$ ns, (b) $t = 1.7$ ns, (c) $t = 1.8$ ns, (d) $t = 1.9$ ns, (e) $t = 2.0$ ns, (f) $t = 2.1$ ns. All vector magnitudes adopt the scale depicted in the legend.

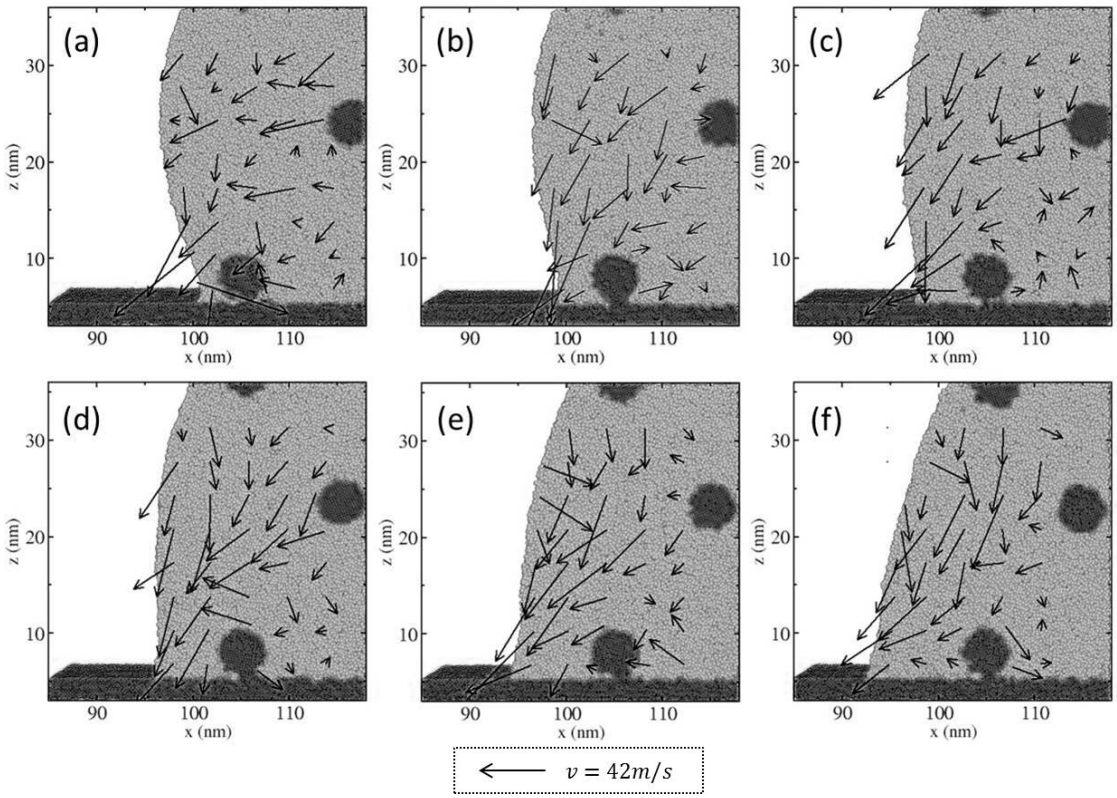

FIG. 9. Data are continued from Fig. 8 with images here showing when the advancing liquid front has detached from the particle and continued to spread forward: (a) $t = 2.2$ ns, (b) $t = 2.3$ ns, (c) $t = 2.4$ ns, (d) $t = 2.5$ ns, (e) $t = 2.6$ ns, (f) $t = 2.7$ ns. All vector magnitudes adopt the scale depicted in the legend.

Figures 8 and 9 show similar data as to what were shown in Fig. 6; however, now a de-pinning case on Cu(001) is explored. Again, behavior observed at the three other de-pinning contact lines were nearly identical to what is presented here. In Fig. 8, contact line behavior leading up to the liquid front detaching from the particle is shown; for all but the last image in Fig. 8, significant flow of liquid lateral to the substrate can be observed. During this time, the particle began forming bonds with the underlying substrate and becoming immobilized. As that happened, flow above the particle caused the contact angle to increase; the largest apparent angle can be observed in Fig. 8e and it is near $120°$; very shortly after this, as shown in Fig. 8f, the liquid front pulls free of the particle. Figure 9 shows that, after the liquid front detaches from the particle, the high

contact angle drives very rapid advancement of the contact line across the surface; Figs. 9a through 9d correspond with the brief period of liquid front acceleration observed in Fig. 4. Figure 9e shows the contact angle has again decreased below $90°$ and Figs. 9e and 9f correspond with the return to decreasing rate spreading kinetics observed for de-pinning systems at $t \geq 2.5$ ns in Fig. 4.

In all cases explored here where particles were entrained into advancing contact lines, the ability for strong chemical bonds to form between particles and the substrate eventually emerged and, as this happened, particle advancement was halted. For wetting on Cu(111) the relatively low advancing contact angle in conjunction with faceting on the entrained particle made it so that, when the particle was halted by the underlying substrate, the liquid was able to adopt the equilibrium contact angle on the faceted particle surface. Since the particle and substrate were of identical chemistry, this is somewhat similar to pinning by a surface roughness feature. For wetting on Cu(001), the contact angle when the particle was halted by the underlying substrate was significantly higher than on Cu(111) such that flow opened up the contact angle further. When the apparent contact angle reached $\sim 120°$ binding between the liquid and the particle was sufficiently reduced for them to separate, leading to de-pinning. Notably, for all cases examined, particles bound to the underlying substrate did not form a clean interface with the surface. The propensity for the liquid to form wetting layers on surfaces of this solid was emphasized by the intrusion of liquid into the interfaces between particles and substrates.

Liquid front behavior and associated flow observed adjacent to the particle during de-pinning in Figs. 8 and 9 indicate that non-trivial capillary and/or drag forces potentially manifest on the particle. Regarding drag on the particle, an important finding was recently advanced for shear flow in a channel past suspended cylinders [35] using both analytical and simulation approaches. Authors of that work found that, when the cylinder was positioned directly adjacent to the channel wall, forces due to drag diminished significantly. Though our flow geometry is different here from the one studied in Ref. 35, sufficient similarity exists that we may expect drag forces to be small, despite the high flow rates observed in Figs. 8 and 9. This is because the cylindrical particles are attached to the substrate and, as described previously, proximity to the solid

surface provides a shielding effect from drag forces.

Regarding capillary force on the particle, expressions advanced in prior studies for such forces involve the product of a relevant length scale (e.g. the pinning particle radius) and the liquid/vapor surface tension; there are typically also geometric factors accounting for contact angle and the shape of the particle [21]. If we simply consider $\gamma_{lv} = 0.574 \pm 0.038$ J / m^2 [23] for the $\phi = 0$ liquid here and multiply that by the particle radius, a force of order 1 nN is obtained. It could be argued that the relevant length scale here is the length of the particle along its cylindrical axis; in that case, the force is twice. While this coarse estimate does not account for contact angle, it provides an idea of the upper bound expected for such forces on particle sizes considered here. Figure 4 permits an alternate interpretation in that one can instead consider the force on the liquid front necessary to cause the deceleration observed during de-pinning. Taking two numerical derivatives of kinetic data in Fig. 4 gives contact line acceleration; comparing acceleration data for de-pinning cases to $\phi = 0$ cases allows extraction of the component of decelerating force associated with the capillary action of the entrained particles on the liquid front. To convert acceleration into force, however, some mass of liquid must be considered to be acted upon during de-pinning and this determination is not obvious. If the mass of liquid so considered is only comprised of those atoms in direct interaction with the particle (i.e. via the underlying interatomic potentials), the peak capillary force so obtained is less than one-tenth of a nano-Newton (nN). This, though, does not seem physically correct when one considers the range of influence observed in the fluid, where flow velocity tens of nano-meters from the contact line is obviously retarded during de-pinning (the cut-off of the atomic interaction functions is of order 0.5 nm). If instead one determines the amount of the drop that would have to be included for the peak force computed to be of order 1 nN (i.e. the upper bound obtained from surface tension considerations), this corresponds to 20% of the droplet atoms; as an upper bound, this seems at least reasonable.

To more directly assess forces manifesting during de-pinning, the collective force on the entrained particle shown in Figs. 8 and 9 was computed; furthermore, forces due to the surrounding liquid were distinguished from forces due to the underlying substrate. To better quantitatively assess such forces, the same calculations were done but for

quiescent situations in which the average forces on the particle were zero. The situations considered were a Cu particle on a Cu substrate, a Cu particle immersed in a Pb(l) at zero flow, and a Cu particle at an interface between a Cu substrate and Pb(l) but for zero flow geometry (see Fig. 10). To compute force on the particle, all atomic forces on particle atoms were summed every 100 simulation steps to obtain a total force on the particle for that time sample. Again, forces due to liquid atoms were distinguished from those due to substrate atoms; furthermore, the x and z components of force were separately computed. To reduce fluctuations, 100 samples were averaged (taken over a consecutive 10000 simulation steps) to obtain a single value reported in force plots in Figs. 10 and 11. For the zero force situations explored in Fig. 10, values obtained can indeed be seen to vary around zero; however, the largest fluctuations observed are of order 1 to 2 nN. If the analysis presented in Fig. 10 is repeated but using 500 sample averaging (i.e. reporting force values computed over 50000 simulation steps), fluctuations are reduced to less than 0.5 nN. Thus, for dynamic wetting simulations, a challenge emerges to maintain high temporal resolution while using sufficient time averaging to reduce fluctuations observed. Given the magnitude of capillary force discussed in the preceding paragraph, fluctuations such as those observed in Fig. 10 indicate it may be difficult to reveal capillary forces definitively from background noise.

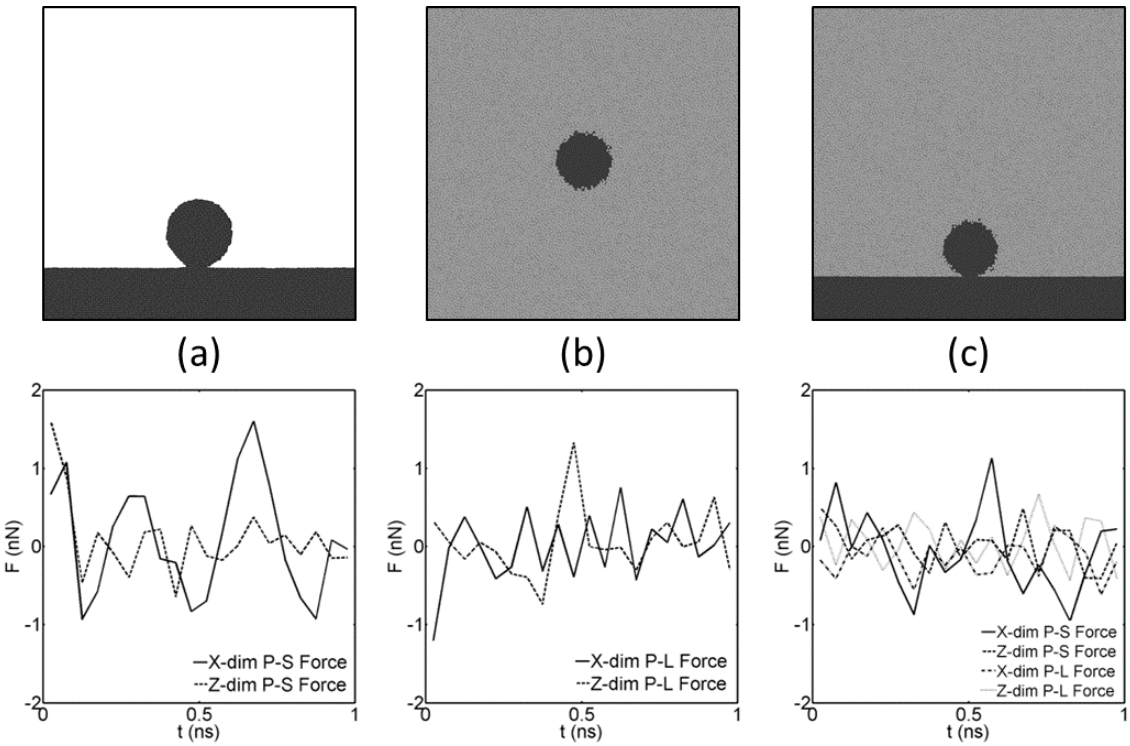

FIG. 10. Force on a particle versus time for three zero force cases: (a) a Cu particle on a Cu substrate, (b) a Cu particle immersed in Pb(l) at zero flow, and (c) a Cu particle at a Cu(001)/Pb(l) interface for zero flow condition. Top images show simulation configurations at t = 1 ns; bottom images show force computed using 100 time sample averages (see text). In legends, P-S is particle/substrate and P-L is particle/liquid.

Using 100 time sample averaging, forces on the particle at the contact line shown in Figs. 8 and 9 were computed during the de-pinning event and results are shown in Fig. 11. The x component forces due to both liquid and substrate remain near zero throughout the analysis, in agreement with drag forces due to liquid flow being relatively small. On the other hand, z component forces exhibited significant deviations from zero, starting at the same time that the droplet begins the de-pinning process. Near $t = 1.3$ ns, the liquid z-component force departed from zero such that the liquid had a net effect of forcing the particle in a direction away from the substrate. Subsequently, for $t \geq 1.4$ ns, the solid z-component force departed from zero with a net effect of forcing the particle toward the substrate. Soon thereafter, for $t \geq 1.7$ ns, the solid and liquid can be seen to exert nearly equal and opposite z-component forces on the particle with magnitudes of order

10 nN and these forces persist after de-pinning is complete. These magnitude forces are clearly larger than fluctuations observed in Fig. 10 so they are statistically significant; however, they are also larger than expected based on coarse estimates of capillary force.

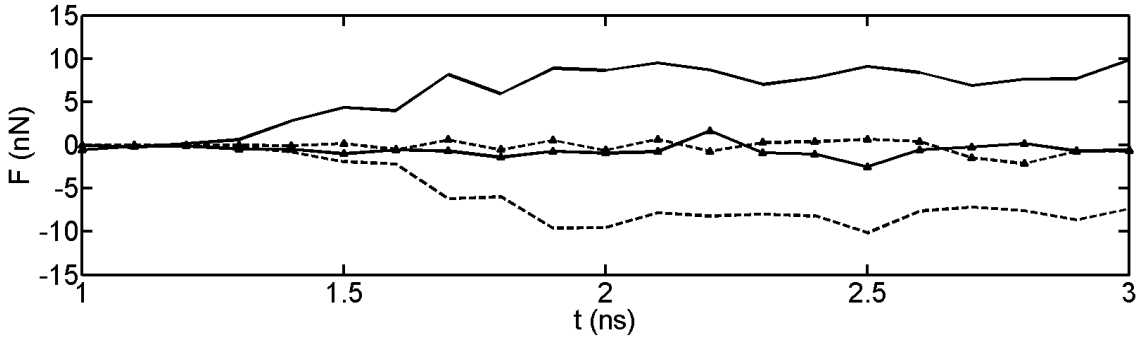

FIG. 11. Force on the particle shown in Figs. 8 and 9. Force components in x (triangles) and z (no symbol) are shown and force exerted on the particle by the liquid (solid curves) is distinguished from force exerted by the substrate (broken curves).

To understand forces computed on the particle during de-pinning, calculations to produce Fig. 11 were repeated but only for the liquid force on the particle. Furthermore, the liquid contributions to force on the particle were distinguished based on geometric considerations. This is perhaps made more clear by horizontal and vertical lines in images shown in Figs. 12 and 13. First, an even division of the particle along the *x* direction was established such that one side could be considered closer to the de-pinning liquid front and the other side could be considered farther from the de-pinning front. Next an approximiate division of the particle into thirds along the *z* direction was established such that one-third of particle atoms could be considered farthest from the substrate, one-third were intermediate distance from the substrate, and one-third were considered adjacent to the substrate. Again, the six regions so established are shown in Figs. 12 and 13. At the start of a 10000 step (100 sample) computation, liquid atoms were divided into groups based on which of the six geometric regions was occupied by a given atom. The force on the particle due to liquid atoms in each region was separately computed and is shown in Figs. 12 and 13 via vector plots. The largest force vector illustrated is 8.3 nN and all vectors are scaled using the same normalization.

As soon as bonds began forming between the particle and substrate, a relatively large force manifested on the region of the particle nearest to the substrate and closer to the detaching liquid front. Surprisingly, the large positive direction z-component force exerted on the particle by the liquid is primarily due to liquid atoms that become essentially trapped at the interface that forms between the particle and the substrate. As shown in Fig. 11, the substrate pulls down on the particle as it attempts to form a clean Cu-Cu interface between particle and substrate. However, liquid atoms trapped at that interface push upward on the particle, producing most of the positive z-component force observed in Fig. 11. For all images in Figs. 12 and 13, the force vector due to liquid in what can be thought of as the lower left region is the largest and it possesses significant postive z-direction character. On the other hand, the force due to liquid in the lower right region, farther from the detaching front, is close to zero throughout the presented analysis. The reason for this is the bonded structure between the particle and the underlying substrate preferentially formed in the region farther from the advancing liquid front; this is apparent in the progression of images shown in Figs. 12 and 13. These observations demonstrate that, for the particle size explored here, forces manifesting on the particle during de-pinning (and afterwards) are dominated by interfacial effects. This is not a surprising result given the very small nano-particles modeled.

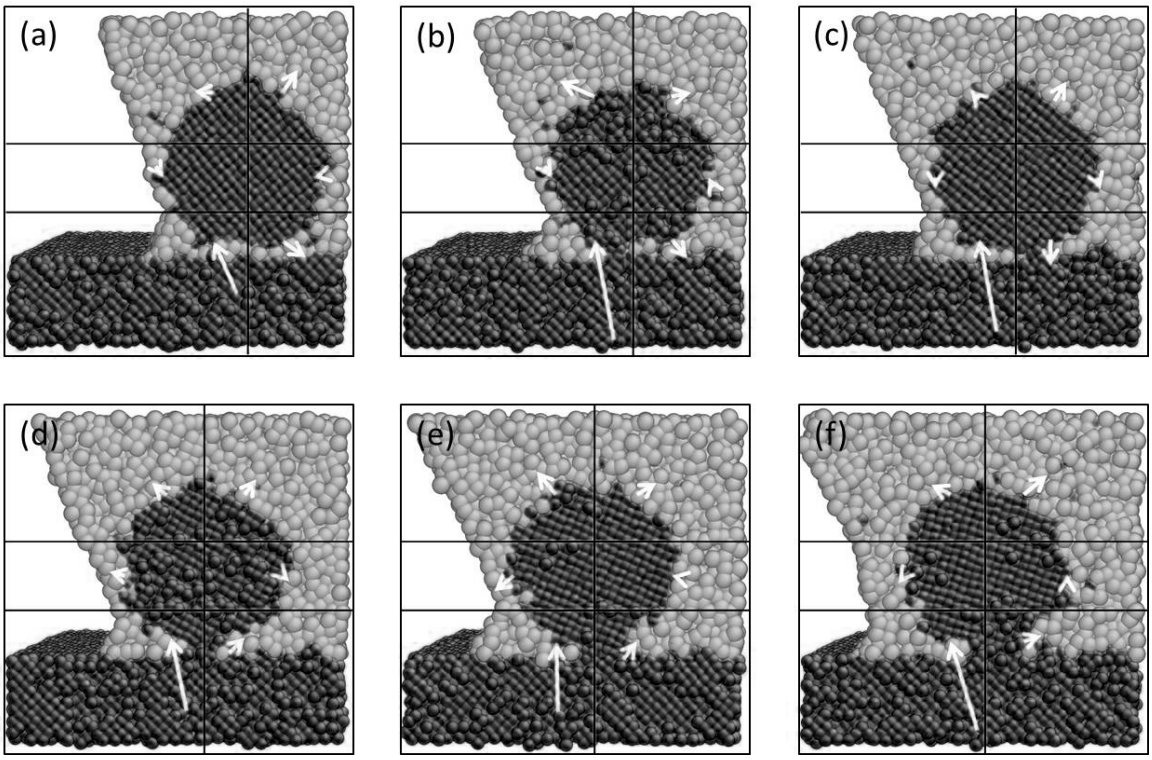

FIG. 12. Force due to liquid atoms on the particle shown in Fig. 8 (also for data in Fig. 11). Force contributions are distinguished based on where in the system liquid atoms are located (as shown by horizontal and vertical dividing lines). The largest vector shown corresponds to 8.3 nN and all vectors are scaled the same. Times shown are the same as in Fig. 8.

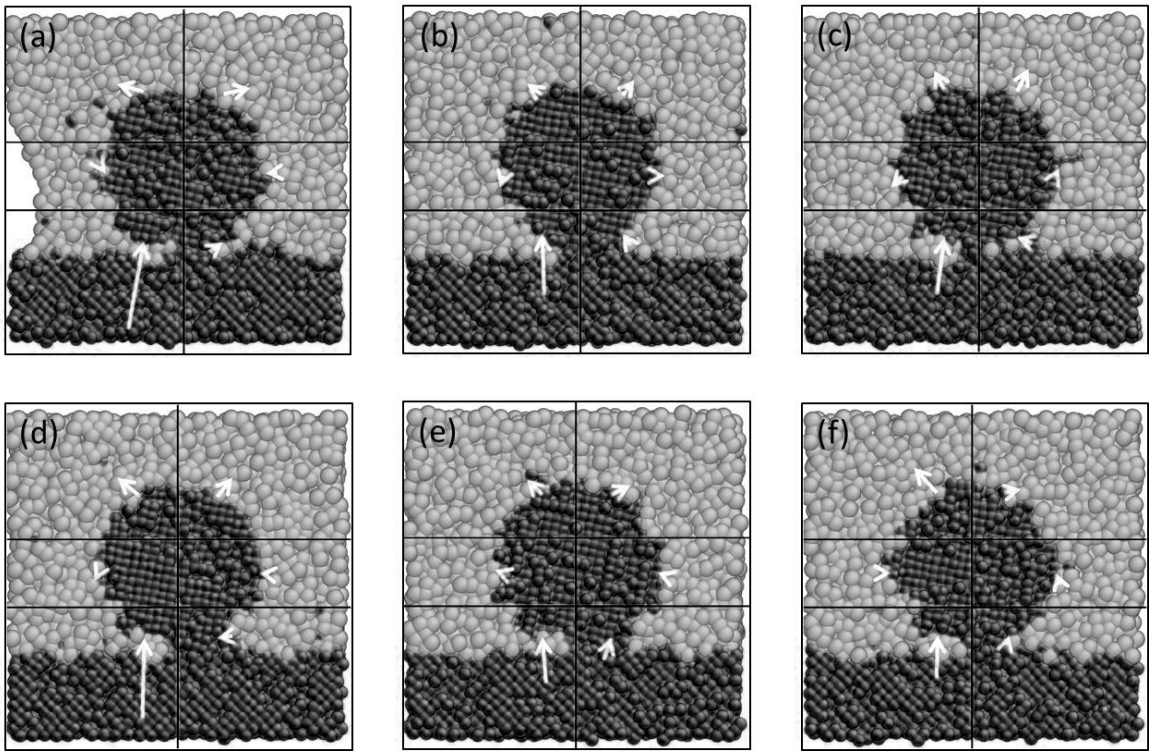

FIG. 13. Force due to liquid atoms on the particle shown in Fig. 9 (also for data in Fig. 11). These images show a continuation from Fig. 12; times shown are the same as in Fig. 9.

Some remaining observations should be made about forces illustrated in Figs. 12 and 13. Though force on the particle is dominated by effects manifesting near the particle/substrate interface, forces due to liquid atoms in the region farthest from the substrate and closer to the advancing liquid front warrant some discussion. These are what can be called the upper left region forces and, in all images in Figs. 12 and 13, those force vectors exhibit a character indicative of lifting the particle away from the substrate and in the direction of liquid front advancement. Magnitudes observed are sufficiently small that drawing quantitative conclusions is not possible; nonetheless, it qualitatively appears that those forces are reflective of either capillary or drag forces (or their combination). A similar argument can be made for forces due to liquid in the middle left region immediately prior to liquid front detachment from the particle. In Figs. 12d and 12e, the force due to liquid in the middle left region is convincingly oriented in the direction of front detachment, which occurs between the times shown in Fig. 12e and Fig.

12f. Though it is again not possible to make quantitative conclusions, these observations lend qualitative support that forces driving pinning and de-pinning can be directly computed in MD simulations. Furthermore, to suppress the dominance of interfacial effects such as observed here, larger particles should be studied.

IV. CONCLUSIONS

Results presented explore pinning and de-pinning events at the atomistic scale during spreading of liquid droplets containing suspended nano-particles. Though fully 3D simulations were employed throughout, both spreading and pinning were reduced to 2D processes by modeling cylindrical drops containing cylindrical particles. The material system modeled was such that, for identical chemistry, varying θ_{adv} was exhibited on different substrate crystallographic orientation surfaces, particularly during early time, inertial stage wetting. For cases where a particle was entrained to an advancing contact line, particles eventually formed strong bonds with the underlying substrate and became fixed at a certain position; following this, self-pinning occured for lower θ_{adv} while de-pinning was observed for higher θ_{adv}.

Pinning in the lower θ_{adv} case was possible because the liquid was able to adopt the equilibrium contact angle for this solid/liquid system on an inclined facet of the pinning particle. In that case, a precursor wetting film that is typically observed for pure drops in this system was still observed to emerge and spread ahead of the pinned droplet edge. Though the precursor film on the substrate surface was an atomic bilayer film; on the particle facet, the liquid film was a monolayer. Thus, percursor kinetics on the substrate were dramatically reduced compared to the pure drop case.

For high θ_{adv}, when an entrained particle became bound to the underlying substrate, flow in the spreading direction caused the contact angle to increase, thereby lowering the capillary force between the particle and the liquid front. Eventually, for $\theta_{adv} \sim 120°$ the liquid front detached from the particle. A computation of forces on entrained particles during de-pinning indicated that, for the small nanoparticles studied here, drag forces due to liquid flow were below the resolution of the force calculation. This is in at least qualitative agreement with recent work [35] examining drag forces on immersed

cylinders for varying separation distance between the cylinder and a substrate surface. In that work, drag forces were demonstrated to diminish dramatically for a cylinder adjacent to a solid surface. Capillary forces, though evident on droplet kinetics during de-pinning, were also below the resolution of our force calculation for particle size studied here. Instead, significant forces manifested on particles during de-pinning in the direction normal to the substrate surface and these were shown to be due to liquid atoms confined between the particle and underlying substrate.

These observations lend confidence that atomic scale simulations can be used to directly compute forces on particles in wetting scenarios and connect those forces to observed behavior near the contact line. It remains an oustanding exercise to determine, for larger particle size, the degree to which more quantitative exploration of drag and capillary forces can also be made. Thus, future work in this area should explore varying particle size as well as higher particle loading so that particle-particle forces can be studied.

This work was supported by the U. S. National Science Foundation, under the Directorate for Engineering, CBET Division (Grant #1512449). Computing and financial resources provided by a Lehigh University Faculty Innovation Grant are also acknowledged.

REFERENCES

[1] T. Young, Philos. Trans. R. Soc. London **95**, 65 (1805).

[2] P. G. de Gennes, Rev. Mod. Phys. **57**, 827 (1985).

[3] D. Bonn, J. Eggers, J. Indekeu, J. Meunier, and E. Rolley, Rev. Mod. Phys. **81**, 739 (2009).

[4] J. H. Snoeijer and B. Andreotti, Annu. Rev. Fluid Mech. **45**, 269 (2013).

[5] A. Stein and R. Schroden, Curr. Opinion in Solid State & Mater. Sci. **5**, 553 (2001).

[6] S. Maenosono, T. Okubo, and Y. Yamaguchi, J. Nanoparticle Research **5**, 5 (2003).

[7] L. Zhang, S. Maheshwari, H.-C. Chang, and Y. Zhu, Langmuir **24**, 3911 (2008).

[8] J. Tang and E. H. Sargent, Adv. Mater. **23**, 12 (2011).

[9] R. D. Deegan, O. Bakajin, T. F. Dupont, G. Huber, S. R. Nagel, and T. A. Witten, Nature **389**, 827 (1997).

[10] R. D. Deegan, Phys. Rev. E **61**, 475 (2000).

[11] R. D. Deegan, O. Bakajin, T. F. Dupont, G. Huber, S. R. Nagel, and T. A. Witten, Phys. Rev. E **62**, 756 (2000).

[12] T. P. Bigioni, X.-M. Lin, T. T. Nguyen, E. I. Corwin, T. A. Witten, and H. M. Jaeger, Nature Mater. **5**, 265 (2006).

[13] A.-M. Cazabat and G. Gu'ena, Soft Matter **6**, 2591 (2010).

[14] H.-S. Kim, S. S. Park, and F. Hagelberg, J. Nanopart. Res. **13**, 59 (2011).

[15] K. L. Maki and S. Kumar, Langmuir **27**, 11347 (2011).

[16] W. Chen, J. Koplik, and I. Kretzschmar, Phys. Rev. E **87**, 052404 (2013).

[17] N. I. Lebovka, S. Khrapatiy, R. Melnyk, and M. Vygornitskii, Phys. Rev. E **89**, 1 (2014).

[18] L. Zhang, Y. Nguyen, and W. Chen, Colloids and Surfaces A: Physicochem. Eng. Aspects **449**, 42 (2014).

[19] D. T. Wasan and A. D. Nikolov, Nature **423**, 156 (2003).

[20] G. Lu, H. Hu, Y. Duan, and Y. Sun, Appl. Phys. Lett. **103**, 253104 (2013).

[21] B. M. Weon and J. H. Je, Phys. Rev. Lett. **110**, 028303 (2013).

[22] V. H. Chhasatia and Y. Sun, Soft Matter **7**, 10135 (2011).

[23] G. Lu, Y.-Y. Duan, and X.-D. Wang, J. Nanopart. Res. **16**, 1 (2014).

[24] S. Cheng and G. S. Grest, J. Chem. Phys. **138**, 064701 (2013).

[25] S. M. Foiles, M. I. Baskes, and M. S. Daw, Phys. Rev. B **33**, 7983 (1986).

[26] H. S. Lim, C. K. Ong, and F. Ercolessi, Surf. Sci. **269/270**, 1109 (1992).

[27] J. J. Hoyt, J. W. Garvin, E. B. Webb III, and M. Asta, Modelling Simul. Mater. Sci. Eng. **11**, 287 (2003).

[28] E. B. Webb III, G. S. Grest, and D. R. Heine, Phys. Rev. Lett. **91**, 236102 (2003).

[29] S. J. Plimpton, J. Comp. Phys. **117**, 1 (1995).

[30] J. Li, Modelling Simul. Mater. Sci. Eng. **11**, 173 (2003).

[31] E. B. Webb III, J. J. Hoyt, G. S. Grest, and D. R. Heine, J. Mater. Sci. **40**, 2281 (2005).

[32] E. B. Webb III and B. Shi, Curr. Opin. Colloid Interface Sci. **19**, 255 (2014).

[33] G. L. J. Bailey and H. C. Watkins, Proc. Phys. Soc., London, Sect. B **63**, 350 (1950).

[34] J. P. Palafox-Hernandez, B. B. Laird, M. Asta, Acta Mater **59**, 3137-44 (2011).

[35] R. Cardinaels, H. A. Stone, Phys. Fluids, **27**, 072001 (2015).

[36] J. F. Lancaster (1965). The metallurgy of welding, brazing and soldering. New York, American Elsevier Pub. Co.

[37] R. Lofting (2014). Brazing and Soldering. Ramsbury, United Kingdom, The Crowood Press Ltd.